Information Technology Laboratory
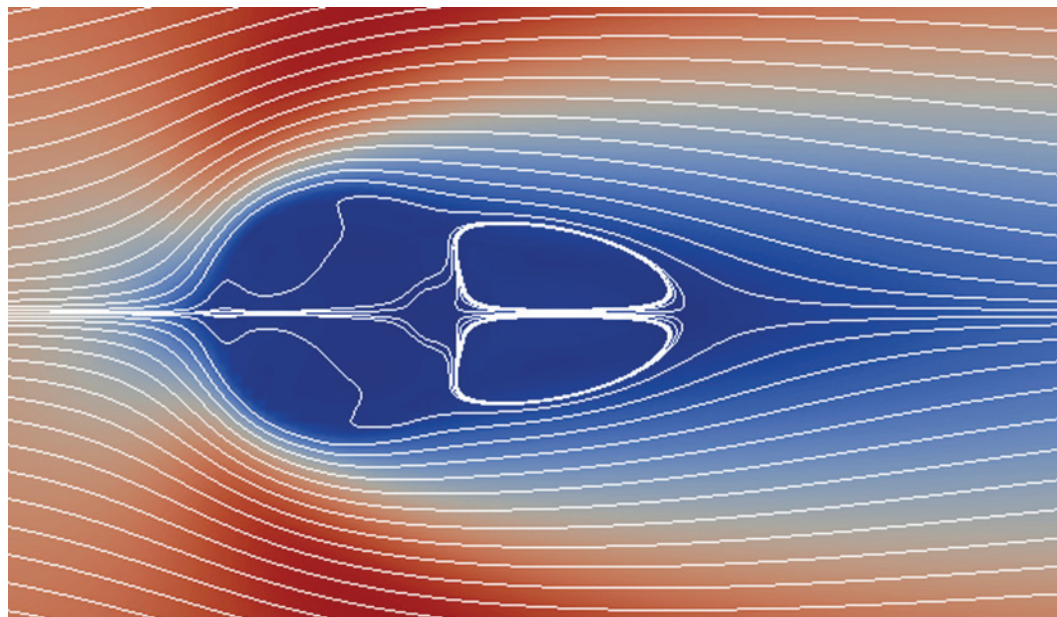
Materials Modeling for Force Protection

Thermal, Microchannel, and Immersed Boundary Extension Validation for the Lattice-Boltzmann Method

Report 2 in "Discrete Nano-Scale Mechanics and Simulations" Series

William P. England and Jeffrey B. Allen   July 2017

The U.S. Army Engineer Research and Development Center (ERDC) solves the nation's toughest engineering and environmental challenges. ERDC develops innovative solutions in civil and military engineering, geospatial sciences, water resources, and environmental sciences for the Army, the Department of Defense, civilian agencies, and our nation's public good. Find out more at www.erdc.usace.army.mil.

To search for other technical reports published by ERDC, visit the ERDC online library at http://acwc.sdp.sirsi.net/client/default.

Thermal, Microchannel, and Immersed Boundary Extension Validation for the Lattice-Boltzmann Method

Report 2 in "Discrete Nano-Scale Mechanics and Simulations" Series

William P. England and Jeffrey B. Allen

Information Technology Laboratory
U.S. Army Engineer Research and Development Center
3909 Halls Ferry Road
Vicksburg, MS 39180-6199

Report 2 of a series

Approved for public release; distribution is unlimited.

Abstract

The Lattice Boltzmann Method continues to garner interest in fluids research, particularly with its ability to accurately simulate laminar flows in the incompressible region. This interest can be attributed in part to the ease of implementation the Lattice Boltzmann Method provides; including a lack of complex differential terms and a linear approximation of the collision operator contained in the Boltzmann equation. In this work, the traditional Lattice Boltzmann solver is augmented with support for immersed boundaries, thermal flows, and microchannel flows. Thermal and micro-enabling support is demonstrated and validated through Rayleigh convection in a square channel and thermally coupled Poiseuille flow through a microchannel, respectively.

Contents

Figures and Tables

Figures

Tables

Preface

Unit Conversion Factors

Multiply	By	To Obtain
Lattice unit (lu)	a constant dependent on scale	Meters (m)

Acronyms and Abbreviations

BGK	Bhatnagar-Gross-Krook
CFD	Computational Fluid Dynamics
DSBC	Diffuse Scatter Boundary Conditions
D2Q9	2-dimentional lattice (D2) with nine discrete velocities (Q9) model
IMB	Immersed Moving Boundary
Kn	Knudsen number
LBE	Lattice Boltzmann Equation
LBM	Lattice Boltzzmann Method
NS	Navier-Stokes method
Nu	Nusselt number
Pr	Prandtl number
Ra	Reynolds number

1   Introduction

1.1   Background

The use of the Lattice Boltzmann Method (LBM) for numerically simulating secondary (amorphous) phase constituents (most often represented as a laminar, incompressible fluid) within the context of material science-based applications is, for these purposes, strategically based on two primary motivations. The first, and possibly the most dominant, relates to the omnipresent problem of spatiotemporal scale compatibility and reconciliation, wherein one attempts to make macroscale material decisions based on microscale or nanoscale performance criteria. The second motivation relates to concerns about the accuracy of the method, particularly with respect to flows over complex geometries.

While the details surrounding these two strategic purposes, including a thorough description of the "pros" and "cons" for using LBM over the more traditional Computational Fluid Dynamics (CFD) techniques are included within the first report of this series (Allen et al. 2014). This first report, in terms of validated examples and algorithm development, provided only an elementary preview into the vast capabilities and sophistication of LBM. The necessary extensions leading ultimately to the resolution of the assigned motivating purposes were left largely unfulfilled. The goal therefore, of this, the second report in the series, is to fulfill these aforementioned purposes, and advance current understanding through a series of verified, algorithmic extensions to the method.

In Allen et al. 2014, an atomistic fluid solving method founded on statistical mechanics and kinetic theory was introduced. The LBM includes no continuum assumption with regard to the flow; rather the fluid is described by individual distribution functions that describe the expectation of finding a particle in some phase and temporal domain (Allen et al. 2014). In this model, macroscopic quantities such as density and velocity are easily computed as velocity moments of the distribution functions. From these moments, nearly all other quantities specific to the LBM can be described. The accuracy of the LBM with respect to macroscopic, isothermal fluid simulations against static, rigid boundaries was demonstrated in Report One through use of a number of benchmark flow cases. It was shown that results of these demonstrations were found to be in very good agreement

with Navier-Stokes (NS) based solutions in all cases, ensuring the validity of the LBM as an accurate fluid solving method. The Lattice Boltzmann Equation (LBE) as presented in Report One is:

$$f_i\left(\vec{x}+\vec{c}_i\hat{\delta}_t, t+\hat{\delta}_t\right) - f_i\left(\vec{x},t\right) = \frac{1}{\tau}\left(f_i\left(\vec{x},t\right) - f_i^{eq}\left(\vec{x},t\right)\right) + \vec{F}_i\delta_t \qquad (1)$$

However, as stated in Report One, a determining factor for the implementation of the LBM was its ability to simulate microscale flows, a feature not often available to more traditional solvers due the to a continuum assumption for the fluid model. Further, it was stated that the LBM is able to more accurately simulate flow against complex geometries due the mesh being of a simpler quality and less computationally expensive.

As stated, this report attempts to address these proposals by providing an updated implementation of the Immersed Moving Boundary (IMB) method made possible by accurately capturing the momentum exchange between particles and fluid interface. Also, this report demonstrates the capacity of the method to support microchannel simulations by introducing an accurate model of the Knudsen layer with Diffuse Scatter Boundary Conditions (DSBC), wherein slip velocity on the channel walls is introduced. With regard to the IMB method, certain properties were desired; specifically, that the flow is able to respond to irregular geometries despite the lattice domain property of the LBM that introduces stair step geometries. Initial rigid boundary implementation should be changed to a dynamic one, able to deform per particle forcing interactions. With such an implementation, complex channels and boundaries can be accurately represented, as are often encountered in computation fluid domains.

With regard to the microscale implementation, the chosen method should accurately account for fluid properties due to rarefaction effects at the microscale. Among these effects, is the presence of Knudsen layer whose existence, in many cases, dominates fluid interactions. Due to higher collision frequency at the wall, the implementation should also be able to simulate a wall slip velocity condition. It is to be shown that the DSBC, whose roots lie in kinetic theory, is suitable for such conditions. Further, implementation of the tangential momentum accommodation coefficient, being a property inherent to the material, allows the DSBC to be extended for modeling not only the aforementioned complex geometries, but also various material types.

1.2 Objective

This report seeks to demonstrate that the accuracy of the LBM is maintained even with the aforementioned, implemented extensions. While Navier-Stokes based solvers tend to dominate CFD related simulations, the LBM has received much interest in recent years, due in part to being able to produce accurate results where Navier-Stokes approximations fail; particularly as a the modeled scale decreases (Allen et al. 2014). In-house developed code compared against international research efforts demonstrate the validity of the current LBM implementation through a variety of popular simulation cases, including; drag coefficient calculations for an immersed cylinder, Rayleigh convection in a square channel, and microscale Poiseuille flow.

1.3 Approach

This second report is intended to serve as an extension to Report One. It was shown in the first report (Allen et al. 2014) that the LBM can return the Navier-Stokes equations using the Chapman-Enskog expansion. While this report does not return implemented contributions to the NS equations, certain NS contributions can be seen in the thermal support equations. Further, microscale implementations step outside the realm of the macroscopically employed NS scenarios and employ concepts derived from kinetic theory, being central to the foundations of the LBM.

2   Immersed Moving Boundary

In this work, support for the IMB is implemented in the LBM to simulate particulate flows for complex moving geometries. The IMB was originally developed by Peskin (2002) for biological simulation of blood flow around the heart and has since quickly evolved into an effective method for fluid-boundary simulation for incompressible flows. This section is validated by applying laminar flow around an immersed cylinder. Like the implementation of the classical LBM, the IMB method follows a similar ease of implementation. No complex or computationally intensive differential terms are needed and the translation from Lagrangian space to Eulerian space is relatively straightforward. Further, implementation results of the IMB with the single relaxation time Bhatnagar-Gross-Krook (BGK) collision remain comparable to multi-relaxation models (Niu et al. 2006).

In the IMB approach, boundary nodes are represented as a mesh of underlying Lagrangian markers able to be moved in continuous space. This contrasts with the discretized Eulerian markers that mark the flow as shown in Figure 1. Once the flow on the Eulerian markers reaches a Lagrangian boundary marker, a calculated force is exerted on the Lagrangian boundary marker, accelerating the boundary and updating its translational and angular velocities. The exerted force on the Lagrangian markers is then pushed back on the Eulerian markers using a carefully chosen mollifier to ensure agreement with Newton's Third Law (Feng and Michaelides 2003; Peskin 2002). Functions that may be categorized as mollifiers must be smooth and the functionally bounded area must be unity. This makes a well-chosen mollifier ideal for reapplying the boundary force onto the flow.

The IMB algorithm procedure occurs as follows:

1. Collide the particles.
2. Add calculated forces to the collisions.
3. Stream updated distribution functions.
4. Update Lagrange markers using Lagrange polynomials.
5. Calculate bounceback contribution at Lagrange points.
6. Update Eulerian mesh using mollifier.
7. Repeat steps 1-6 until convergence.

Figure 1. Non-rigid Lagrangian mesh imposed over Eulerian mesh.
The dark, hollow points represent Langrangian nodes, while
vertices of coordinate lines represent Eulerian nodes.
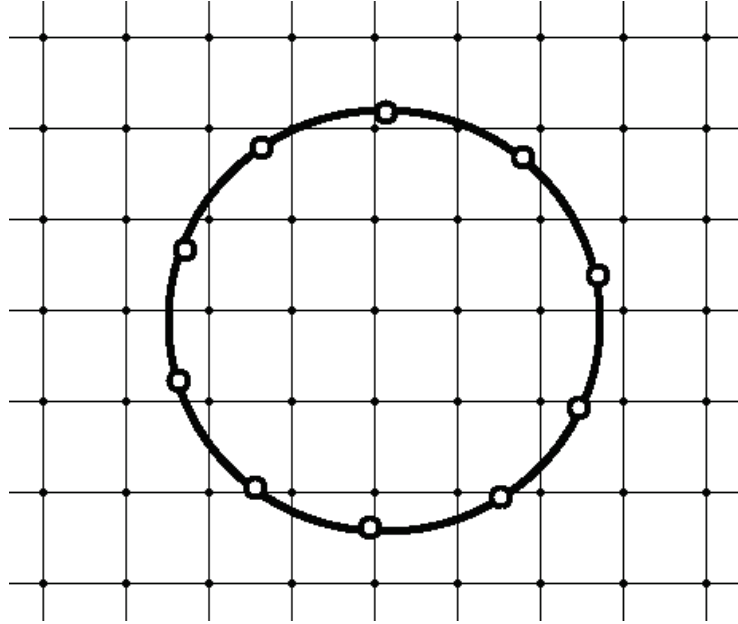
As shown by Equation. 1, the LBM allows the addition of external forces. In the IMB, the external force is the force that is exerted by the Lagrangian mesh onto the Eulerian mesh. While there are many schemes to add an external force to the LBM equations, in this work, the force adding scheme demonstrated by Mohamad et al. (2010), as shown in Equation 2 is applied.

$$ f_b = \frac{w_i}{c_s}\left(\vec{F_i} \cdot \vec{c_i} \right) \tag{2} $$

This requires the force to be split into eight separate elements (F_0 is always zero due to $\vec{c_0}$) to be added to the respective distribution functions. As previously mentioned, the single relaxation time BGK collision term is used throughout this work. After colliding the particles, the force is then added as previously shown. The particles are then streamed across the Eulerian markers.

To represent the boundary locations, Lagrangian markers are placed at $\vec{X_s}$ for $s \,\epsilon\, \Omega$ where Ω is the fluid domain, s represents the sth marker, and $\vec{X_s}$ is the position of that marker at $\vec{X_s}(X_s, Y_s)$. Note that, in this work, capital letter quantities are used to represent Lagrangian quantities while lowercase letter quantities represent Eulerian quantities.

To calculate the distribution functions at a Lagrangian marker, two-dimensional Lagrange interpolation is employed on the surrounding Eulerian markers by Equation 3. Here, interpolate all Lagrangian marker distribution functions accurate to the third order.

$$f_\alpha\left(\vec{X}_s,t\right)=\sum_{ij}\left(\prod_{k=1,k\neq i}^{i_{tot}}\frac{X_s-x_{kj}}{x_{ij}-x_{kj}}\right)\left(\prod_{m=1,m\neq j}^{j_{tot}}\frac{Y_s-y_{im}}{y_{ij}-y_{im}}\right)f_\alpha\left(\vec{x}_{ij},t\right) \qquad (3)$$

Once the distribution functions have been interpolated, they are updated using the bounceback scheme (Zou and He 1997) presented in Equation 4 to ensure a no-slip condition on the boundary, where β is the opposite direction of α or $\vec{c}_\beta = -\vec{c}_\alpha$ and $\vec{u}_{tot}$ is the total velocity written in terms of the translational velocity, $\vec{u}_0$, and the angular velocity, $\vec{\omega}_0$, shown in Equation 4.1.

$$f_\beta\left(\vec{X}_s,t+\delta_t\right)=f_\alpha\left(\vec{X}_s,t\right)-2w_\alpha\rho\frac{\vec{c}_\alpha\cdot\vec{u}_{tot}}{c_s^2} \qquad (4)$$

where

$$\vec{u}_{tot}=\vec{u}_o+\vec{\omega}_o\times\left(\vec{X}_s-\vec{X}_{cm}\right) \qquad (4.1)$$

The force density, $\vec{F}_s(\vec{X}_s,t)$ at $\vec{X}_s$ that is to be exerted on the nearby Eulerian markers is calculated by Equation 5. The difference in the opposite distribution functions is representative of a momentum exchange between the particles that results in a change in the boundary's velocity. The direction of $\vec{F}_s$ is determined by the magnitude of this exchange when multiplied by the lattice velocity.

$$\vec{F}_s\left(\vec{X}_s,t\right)=\sum_\beta\vec{c}_\beta\left[f_\beta\left(\vec{X}_s,t\right)-f_\alpha\left(\vec{X}_s,t\right)\right] \qquad (5)$$

With $\vec{F}_s(\vec{X}_s,t)$ calculated, the force can now be distributed to the flow through the use of the aforementioned mollifier. The total force redistributed to the flow is given by Equation 6.

$$\vec{F}_r\left(\vec{r},t\right)=\int_\Omega\vec{F}_s\left(\vec{X}_s,t\right)\delta\left(\vec{r}-\vec{X}\right)ds \qquad (6)$$

where δ_h is the chosen mollifier. In his work, Peskin (2002) presented two delta functions for δ_h, shown in Equation 7 and Equation 8.

$$\delta_h(x) = \begin{cases} 0, x \leq -2 \\ \dfrac{1}{8}\left(5 + 2x - \sqrt{-7 - 12x - 4x^2}\right), -2 \leq x \leq -1 \\ \dfrac{1}{8}\left(3 + 2x + \sqrt{1 - 4x - 4x^2}\right), -1 < x \leq 0 \\ \dfrac{1}{8}\left(3 - 2x + \sqrt{1 + 4x - 4x^2}\right), 0 < x \leq 1 \\ \dfrac{1}{8}\left(5 - 2x - \sqrt{-7 + 12x - 4x^2}\right), 1 < x \leq 2 \\ 0, 2 \leq x \end{cases} \tag{7}$$

$$\delta_h(x) = \begin{cases} \dfrac{1}{4}\left(1 + \cos\left(\dfrac{\pi x}{2}\right)\right), |x| \leq 2 \\ 0, \text{otherwise} \end{cases} \tag{8}$$

Applying $\delta_h(x)$ to both the x and y Eulerian coordinates yields Equation 9. The effective force distribution geometry is a square where the Lagrangian marker is located at the center and the length of the sides is two for both Equation 7 and Equation 8. In this work, Equation 8 is used exclusively primarily due to ease of implementation without loss of accuracy (Appendix A).

$$D_{ij}\left(\vec{r}_{ij} - \vec{X}_s\right) = \frac{1}{\delta_x^2} \delta_h\left(\frac{x_{ij} - X_s}{\delta_x}\right) \delta_h\left(\frac{y_{ij} - Y_s}{\delta_x}\right) \tag{9}$$

Independent of the mollifier, because the fluid domain is discretized into Eulerian markers with constant spacing δ_x, Equation 6 must be discretized accordingly. (It is important to note that summing the mollifier on discrete steps of Δx still sums to unity, proving that no magnitude of force is lost in redistribution to the flow. See Appendix A for a more formal proof of this). Placing Equation 9 into Equation 6 yields the final force distribution.

$$\vec{F}_r\left(\vec{r}_{ij}, t\right) = \sum_s \vec{F}_s\left(\vec{X}_s, t\right) D_{ij}\left(\vec{r}_{ij} - \vec{X}_s\right) \Delta l_s \tag{10}$$

2.1   Object properties

In this implementation of the IMB, Lagrange markers are initialized with a link to the nearest Lagrange markers for quick access to information contained by surrounding Lagrange nodes. Following this, it is possible to start at an arbitrary Lagrange marker and follow its links to many other Lagrange nodes. The term *object* is applied to the collection of such a group of linked Lagrange markers. Further, this linking scheme allows the possibility to create as many objects as desired which are able to interact with other objects with little description of object interaction.

In this implementation, each Lagrange marker is weighted by a mass m_s, such that an object's mass is: $m_o = \sum_s m_s$. The first moment of mass divided by m_o is shown in Equation 11 and provides the location of the center of mass of the object.

$$\vec{X}_{cm} = \frac{1}{m_o}\sum_s m_s \vec{X}_s \tag{11}$$

To obtain the total force on an object, simply sum the balance force of the respective Lagrange markers' forces contained by the object as shown in Equation 12.

$$\vec{F}_o = -\sum_s \vec{F}_s \tag{12}$$

This now allows the opportunity to turn to Newton's Second Law to calculate the translational velocity of an object, provided in Equation 13.

$$d\vec{u}_o = \frac{\vec{F}_o dt}{m_o} \tag{13}$$

Similarly, the total torque on the object is given by Equation 14. Note that the torque acts in the third dimension, and is not present in the 2-dimentional lattice (D2) with nine discrete velocities (D2Q9) model (Allen et al. 2014).

$$\vec{T}_o = \sum_s (\vec{X}_s - \vec{X}_{cm}) \times \vec{F}_s\left(\vec{X},t\right) \tag{14}$$

The moment of inertia, I_o, is given by

$$I_o = m_s(\vec{X}_s - \vec{X}_{cm})^2 \qquad (15)$$

From the object's torque and moment of inertia, the angular velocity can be obtained, which is shown in Equation 16.

$$d\vec{\omega}_o = \frac{\vec{T}_o dt}{I_o} \qquad (16)$$

Finally, considering both the translational and angular velocity contributions, the total velocity is calculated by Equation 4.1.

In this implementation, the object is able to rotate about its center of mass. This is accomplished by employing the rotation matrix shown in Equation 17, where θ is given in Equation 18.

$$R = \begin{pmatrix} \cos\theta & \sin\theta \\ -\sin\theta & \cos\theta \end{pmatrix} \qquad (17)$$

$$d\theta = \vec{\omega}_o dt \qquad (18)$$

The parameter $\vec{X}_s'$ denotes the new location of Lagrange marker $\vec{X}_s$ after rotation and is given by Equation 19.

$$\vec{X}_s' = R(\vec{X}_s - \vec{X}_{cm}) + \vec{X}_{cm} \qquad (19)$$

2.2 Validation

To validate the computational accuracy of the IMB method, laminar flow across an immersed cylinder is considered. This flow problem has been studied extensively and has been shown to preserve accuracy in the LBM. (Niu et al. 2006). However, this problem can be difficult to model effectively due to the *stair step* geometry imposed on boundary walls by lattice discretization. The IMB method remediates this problem due to the boundary being composed of Lagrangian markers with no ties to any specified Eulerian marker. One common measurement of flow around an immersed cylinder is the drag coefficient C_D. This quantity may be defined in terms of the streamwise component of the force acting on the boundary by $C_D = \frac{F_x}{\rho_{avg} u_0^2 r}$, where u_0 is the inlet stream velocity and r is the radius of the cylinder.

To set up this simulation, the cylinder was initially placed at $\vec{x} = \left(\frac{2}{5}L, \frac{1}{2}H\right)$, where L and H are the length and height of the channel, respectively. A prescribed velocity of u_0 is set at the inlet. The top and bottom walls are treated by standard no-slip bounceback conditions and the outlet density is extrapolated from nearby lattice sites. Further, the size of the channel is defined by $L = 8or$ and $H = 8or$. It can be seen in Figure 2 that two vortices develop behind the object. The x-wise length, or recirculation length, of the vortices can be expressed in terms of the radius of the cylinder by $L_w = \frac{4L_r}{r}$, where L_r is the measured recirculation length. Results of yielded drag coefficient and recirculation for Re = 20 are compared with other LBM implementations by Niu et al. (2006) and He et al. (1998) and are presented in Table 1.

Figure 2. Flow around and immersed cylinder for Re = 20.
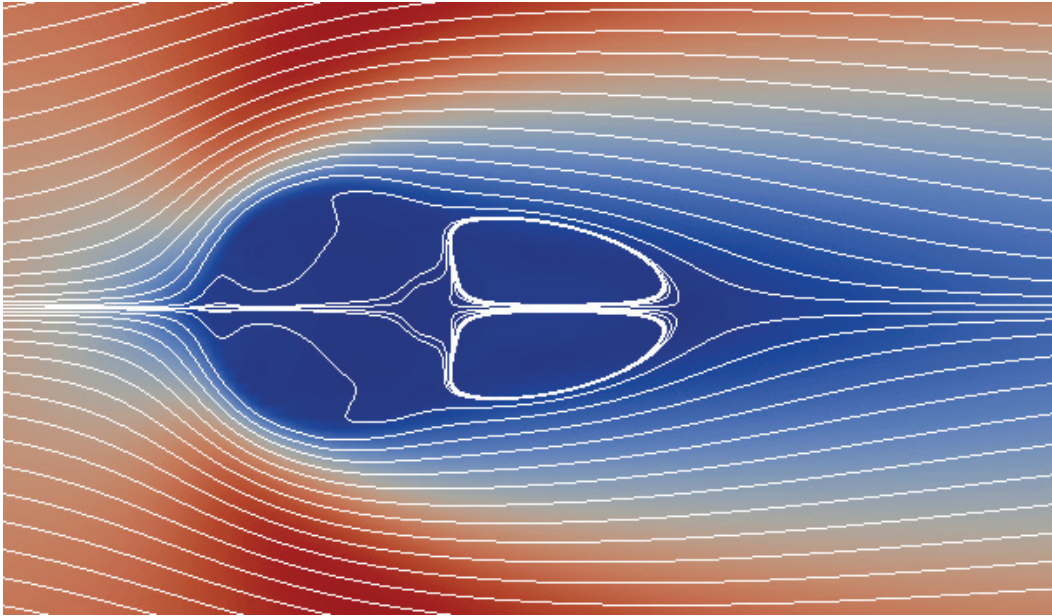
Table 1. Drag coefficient and recirculation length comparison for Re = 20.

	C_D	Abs. Error	L_w	Abs. Error
Niu et al.	2.144	-	1.89	-
He et al.	2.152	0.373	1.84	2.645
Current	2.259	5.363	1.95	3.174

3 Thermal Interactions

Thermal support in the LBM has been an area of interest for accurate simulation of thermal particulate interaction for various scales and has led to the development of thermal implementation methods. Among these methods are the multispeed method (McNamara et al. 1995), the passive scalar method (Shan 1997) and the thermal energy distribution function method (He et al. 1998).

The multispeed method extends the LBM equation to include calculations of macroscopic temperature through implementation of new, higher order velocity terms. While the multispeed approach may be straightforward for the LBM, results from this method are often unstable. Further, the range of supported temperatures is limited. (McNamara et al. 1995)

The passive scalar method implements thermal support by introducing a second distribution function to simulate thermal interactions. This method assumes that viscous heat dissipation and compression work done by the pressure can be ignored, but does suffer from the same numerical instability as the multispeed method.

In this work, the thermal energy distribution function method proposed by He et al. (1998) is implemented. Following the work done by Peng et al. (2003), the thermal energy distribution function is simplified by neglecting the compression work done by the pressure and the viscous heat dissipation. Eliminating these contributions is a stipulation also imposed by the aforementioned passive scalar method and are justified in incompressible fluid interaction as described by Peng et al. (2003) Further, these contributions are contained in a complex gradient term that complicates the LBM and was shown by Peng et al. (2003) to double computation time in many situations.

The density distribution function and thermal distribution functions as per the work of He et al. (1998) are presented in Equations 20 and 21.

$$\overline{f}_i\left(\vec{x}+\vec{c}_i\hat{\delta}_t, t+\hat{\delta}_t\right) - \overline{f}_i\left(\vec{x},t\right) = -\frac{\delta_t}{\tau_v + \frac{1}{2}\delta_t}\left[\overline{f}_i\left(\vec{x},t\right) - f_i^{eq}\left(\vec{x},t\right)\right] + \frac{\tau_v F_i \delta_t}{\tau_v + \frac{1}{2}\delta_t} \qquad (20)$$

$$\bar{g}_i\left(\vec{x}+\vec{c}_i\hat{\delta}_t,t+\hat{\delta}_t\right)-\bar{g}_i\left(\vec{x},t\right)=-\frac{\delta_t}{\tau_c+\frac{1}{2}\delta_t}\left[\bar{g}_i\left(\vec{x},t\right)-g_i^{eq}\left(\vec{x},t\right)\right]+\frac{\tau_c f_i\left(\vec{x},t\right)q_i\delta_t}{\tau_c+\frac{1}{2}\delta_t} \quad (21)$$

where $\bar{f}_i$ and $\bar{g}_i$ are the new distribution functions introduced by He et al. (1998) and are written in terms of f_i and g_i, where f_i is the traditional density distribution function and g_i is the thermal distribution function and q_i represents the viscous heating and compression work. The respective relaxation times are now denoted as τ_v and τ_c for the density and thermal distribution functions, respectively. Also proposed by He et al. (1998) are related, but simpler functions, shown in Equations 22 and 23.

$$\bar{f}_i = f_i + \frac{\delta_t}{2\tau_v}\left(f_i - f_i^{eq}\right)-\frac{\delta_t}{2}F_i \quad (22)$$

$$\bar{g}_i = g_i + \frac{\delta_t}{2\tau_v}\left(g_i - g_i^{eq}\right)-\frac{\delta_t}{2}f_iq_i \quad (23)$$

where F_i is the distribution of a force $\vec{G}$ acting on the system and the force adding scheme is applied in the collision step by

$$F_i = \frac{\vec{G}\cdot\left(\vec{c}_i-\vec{u}\right)}{RT}f_i^{eq} \quad (24)$$

The q_i term in Equation 23 contributes to recovering the viscous heating and compression work done by the pressure and is written as

$$q_i = \left(\vec{c}_i-\vec{u}\right)\cdot\left[\frac{1}{\rho}\left(-\nabla p+\nabla\cdot\Pi\right)+\left(\vec{c}_i-\vec{u}\right)\cdot\nabla\vec{u}\right] \quad (25)$$

where the stress tensor

$$\Pi = \rho v\left(\nabla\vec{u}+\vec{u}\nabla\right) \quad (26)$$

The introduction of $\bar{f}_i$ and $\bar{g}_i$ seeks to repair an inconsistent viscosity calculation among the two distribution functions, as exposed by Chapman-Enskog multiscale expansion (Peng et al. 2003). However, because of the negligible effect of viscous heating for incompressible flows, the following simplified thermal energy distribution proposed by Peng et al. (2003) can

be shown to preserve computational accuracy by eliminating the complex gradient calculations in Equation 25, and, by extension, the necessity of $\bar{f}_i$ and $\bar{g}_i$.

Peng et al.'s (2003) simplified thermal distribution functions follows the same evolution as the density distribution function and is presented as

$$g_i\left(\vec{x}+\vec{c}_i\hat{\delta}_t,t+\hat{\delta}_t\right)-g_i\left(\vec{x},t\right)=\frac{1}{\tau_c}\left(g_i\left(\vec{x},t\right)-g_i^{eq}\left(\vec{x},t\right)\right) \tag{27}$$

The new distribution function presented in Equation 27 follows the same collision and streaming evolution as the classic LBM. For the thermal distribution function, the internal energy is represent by $\varepsilon = \frac{DRT}{2}$, where $D = 2$ for two dimensions and is calculated as

$$\rho\varepsilon = \sum_i g_i \tag{28}$$

The macroscopic temperature can then be extracted by solving Equation 28 for T. In D2Q9, the equilibrium thermal distribution is given by

$$g_0^{eq} = -\frac{2\rho\varepsilon}{3}\frac{\vec{u}^2}{c^2}$$

$$g_{1,2,3,4}^{eq} = \frac{\rho\varepsilon}{9}\left[\frac{3}{2}+\frac{3}{2}\frac{\vec{c}_i\cdot\vec{u}}{c^2}+\frac{9}{2}\frac{\left(\vec{c}_i\cdot\vec{u}\right)^2}{c^4}-\frac{3}{2}\frac{\vec{u}^2}{c^2}\right] \tag{29}$$

$$g_{5,6,7,8}^{eq} = \frac{\rho\varepsilon}{36}\left[3+6\frac{\vec{c}_i\cdot\vec{u}}{c^2}+\frac{9}{2}\frac{\left(\vec{c}_i\cdot\vec{u}\right)^2}{c^4}-\frac{3}{2}\frac{\vec{u}^2}{c^2}\right]$$

In the simplified thermal energy distribution model, the viscosity is consistent across both distribution function and is given by

$$v=\left(\tau_v-\frac{1}{2}\right)c_s^2\delta_t \tag{30}$$

Another parameter of interest is the thermal diffusivity, X, and it is related to the thermal relaxation time by

$$X = \frac{2}{3}\left(\tau_c - \frac{1}{2}\right)c^2\delta_t \tag{31}$$

3.1 Boundary conditions

Correct implementation of boundary conditions is especially important for the thermal distribution function method due to the addition of a second distribution function. In their work, Liu et al. (2010) applied a density boundary condition shown along a single wall. In this work, such a boundary condition is applied and is presented for the case of a general wall as reformulated by the authors. In this scheme, the unknown density distribution functions are given as

$$f_\sigma = f_\sigma^* + \frac{w}{c}\left(\vec{c}\cdot\vec{Q}\right) \tag{32}$$

where $\vec{Q} = \left(Q_x\,\vec{x}, Q_y\,\vec{y}\right)$ and acts as a force corrector to enforce the desired momentum on the boundary and f_σ^* is a value to be chosen and is usually represented by an approximation to f_σ. In this work, $f_\sigma^* = f_\sigma^{eq}$, and σ represents the set of the three unknown distribution function indexes on the wall such that $\sigma = \{\alpha, \beta, \gamma\}$. Following the traditional formulation for ρ and $\vec{u} = (u\,\vec{x}, v\,\vec{y})$ and assuming that u and v on the wall are known, ρ, Q_x, and Q_y can be solved by setting up the following linear system:

$$\begin{pmatrix} 1 & -k_x & -k_y \\ u & -k_{xx} & -k_{xy} \\ v & -k_{xy} & -k_{yy} \end{pmatrix}\begin{pmatrix} \rho \\ Q_x \\ Q_y \end{pmatrix} = \begin{pmatrix} f^\dagger \\ f_x^\dagger \\ f_y^\dagger \end{pmatrix} \tag{33}$$

$$\begin{aligned} f^\dagger &= \sum_i f_i + \sum_\sigma \overline{f}_\sigma \\ f_x^\dagger &= \sum_i f_i c_{ix} + \sum_\sigma \overline{f}_\sigma c_{\sigma x} \\ f_y^\dagger &= \sum_i f_i c_{iy} + \sum_\sigma \overline{f}_\sigma c_{\sigma y} \end{aligned} \tag{34}$$

$$k_x = \sum_\sigma w_\sigma c_{\sigma x}$$

$$k_y = \sum_\sigma w_\sigma c_{\sigma y}$$

$$k_{xx} = \sum_\sigma w_\sigma c_{\sigma x}^2 \qquad (35)$$

$$k_{yy} = \sum_\sigma w_\sigma c_{\sigma y}^2$$

$$k_{xy} = \sum_\sigma w_\sigma c_{\sigma x} c_{\sigma y}$$

where w_σ is the σth weight determined using the D2Q9 template, $\bar{f}_\sigma = f_\sigma - f_\sigma^*$, and f_σ is the yet to-be-updated σ^{th} function value. It is important to note that this formulation for f_σ on the wall is derived using only Equation 32, $\rho = \sum_i f_i$ and $\rho\vec{u} = \sum_i \vec{c}_i f_i$. Using Equation 34 and Equation 35, values for ρ, Q_x, and Q_y can be determined exactly by any preferred linear system solving method. For the special case of $u = v = 0$, A^{-1} becomes

$$A^{-1} = \begin{pmatrix} 1 & \dfrac{k_y k_{xy} - k_x k_{yy}}{k_{xx} k_{yy} - k_{xy}^2} & \dfrac{k_x k_{xy} - k_y k_{xx}}{k_{xx} k_{yy} - k_{xy}^2} \\[4mm] 0 & \dfrac{-k_{yy}}{k_{xx} k_{yy} - k_{xy}^2} & \dfrac{k_{xy}}{k_{xx} k_{yy} - k_{xy}^2} \\[4mm] 0 & \dfrac{k_{xy}}{k_{xx} k_{yy} - k_{xy}^2} & \dfrac{-k_{xx}}{k_{xx} k_{yy} - k_{xy}^2} \end{pmatrix} \qquad (36)$$

Note that for all non-corner nodes, $k_{xy} = 0$, thus yielding Equation 37

$$A^{-1} = \begin{pmatrix} 1 & \dfrac{-k_x}{k_{xx}} & \dfrac{-k_y}{k_{yy}} \\[4mm] 0 & \dfrac{-1}{k_{xx}} & 0 \\[4mm] 0 & 0 & \dfrac{-1}{k_{yy}} \end{pmatrix} \qquad (37)$$

Equation 37 is applied to all walls in the simulation involving Rayleigh convection. At the corner nodes, the non-equilibrium bounceback condition must be satisfied:

$$f_\alpha^{neq} = f_\beta^{neq} \qquad (38)$$

where $f_i^{neq} = f_i^{eq} - f_i$ and again $\vec{c}_\alpha = -\vec{c}_\beta$. Because f_5 and f_7 for the top left and bottom right corners and f_6 and f_8 for the bottom left and top right corners do not stream into the system (Figure 3), yet contribute to the density of the corner nodes, they are set to their respective equilibrium function values.

Figure 3. Example of non-streaming lattice velocity directions in the D2Q9 model for the top left channel corner. It follows that for the bottom left and top right corners, lattice velocities 6 and 8 directions do not stream.
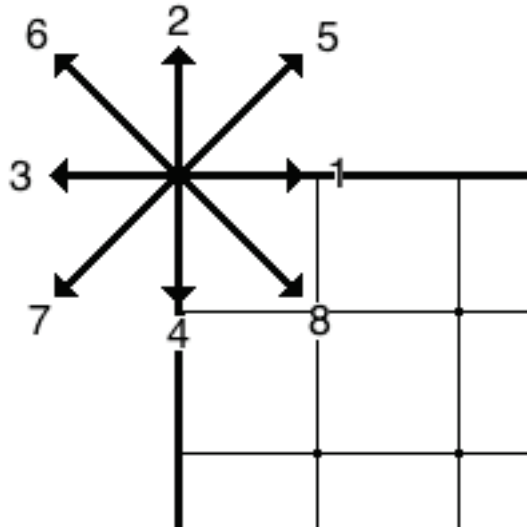
If the temperature on the wall is known, the thermal boundary conditions, presented by Liu et al. (2010), are similar to the density conditions. For this case, the three unknown thermal distribution functions are given by

$$g_\sigma = g_\sigma^* + w_\sigma G_c \tag{39}$$

The set of distribution functions, g_σ^*, are determined arbitrarily (In this work, $g_\sigma^* = g_\sigma^{eq}$). Because the temperature on the wall is known, it follows that

$$\rho\varepsilon = RT_k = \sum_i g_i - \sum_\sigma g_\sigma + \sum_\sigma (g_\sigma^* + w_\sigma G_c) \tag{40}$$

where T_k is the known temperature and σ again represents the set of the unknown distribution function indices. The quantity $\rho\varepsilon^*$ is represented as

$$\rho\varepsilon^* = \sum_i g_i - \sum_\sigma g_\sigma + \sum_\sigma g_\sigma^* \qquad (41)$$

With Equation 40 K, G_c is determined by

$$G_c = \frac{\rho\varepsilon - \rho\varepsilon^*}{\sum_\sigma w_\sigma} \qquad (42)$$

thus allowing solutions of the unknown wall distribution functions from Equation 39.

For walls where the temperature is unknown, a second order Taylor series expansion is applied. To obtain the temperature on the wall, the temperature of the two closest normal nodes and the local rate of change of the temperature in the normal direction are required. On the bottom wall, for example, the temperature is given by

$$T_{0,j} = \frac{2}{3}\frac{\partial T_{0,j}}{\partial y}\delta_y + \frac{4}{3}T_{1,j} - \frac{1}{3}T_{2,j} \qquad (43)$$

where δ_y is the lattice spacing. Once the temperature on the wall marker is determined, the values of the three unknown distribution functions can be found from Equations 39–42.

3.2 Validation

In this work, thermodynamically driven convection was simulated to demonstrate computational validity for the thermal energy distribution method. Natural convection has been shown to be a conventional method to simulate thermal flows and is an attractive validation case due to ease of implementation (Nor Azwadi et al. 2006; Guo et al. 2007; He et al. 1998; Liu et al. 2010; Peng et al. 2003; Shu et al. 1997).

Here, a square chamber of particles, initially at rest, is introduced with the left wall maintained at a high temperature, T_1, and the right wall maintained at a low temperature, T_0. The top and bottom walls are assumed to be adiabatic, such that $\frac{\partial T}{\partial y} = 0$. The temperature difference between the two walls introduces a temperature gradient in the system. Convection occurs when a newly introduced dimensionless parameter, the

Rayleigh number, Ra, is above a critical value causing the system to tend toward thermal equilibrium.

Many studies of Rayleigh convection are examined under the Boussinesq approximation, which assumes that the thermal expansion coefficient, β, and the viscosity, v, are constant. Under this assumption, the buoyancy force acting on the system is given as

$$\rho \vec{G} = \rho \beta g_0 \left(T - T_m\right) \vec{j} \tag{44}$$

where g_0 is the acceleration due to gravity, T_m is the static average temperature given by $T_m = \frac{T_1 + T_0}{2}$, and $\vec{j}$ is the unit vector pointing in the opposite direction of gravity. Two other important quantities are the dimensionless Rayleigh, Ra, and Prandtl, Pr, numbers given as

$$Ra = \frac{\beta g_0 \Delta T H^3}{v \mathrm{X}} \tag{45}$$

$$Pr = \frac{v}{\mathrm{X}} \tag{46}$$

where $\Delta T = T_1 - T_0$ and H is the height of the channel. To test validity of the method the Prandtl number is set to $Pr = 0.71$ allowing for simulation of many gases. The study is conducted over a set of fixed Ra. In this work, the incompressibility constraint (less than 5% mass loss) is determined by the value of $\beta g_0 \Delta T H$. Setting $\beta g_0 \Delta T H$ to a sufficiently small value will maintain the system within the incompressible limit and is chosen per the Rayleigh number.

Once the value of Pr and Ra is chosen, v and X can be determined by Equations 45 and 46. With v and X, τ_v and τ_c are then determined by Equations 30 and 31, respectively.

The Nusselt number, Nu, is another important dimensionless parameter that describes convective heat transfer. Its average value, $\overline{Nu}$, is given by

$$\overline{Nu} = \frac{H}{\mathrm{X}\Delta T} \frac{1}{H^2} \int_0^H \int_0^H q_x\left(x,y\right) dx dy \tag{47}$$

$$q_x(x,y)=u_x T(x,y)- X \frac{\partial T(x,y)}{\partial x} \tag{48}$$

On the boundary, Liu et al. (2010) velocity conditions per Equation 37 are applied with all wall velocities set to zero. Similarly, the right and left thermal boundaries employ the known temperature condition set to T_1 and T_0, respectively. For the top and bottom walls, an adiabatic condition is applied. The temperature is extrapolated following the second order Taylor scheme shown in Equation 40. To ensure the wall is adiabatic, $\frac{dT_w}{dy}$ is set to zero, where T_w is the temperature on the walls.

To demonstrate the validity of the simulation, the obtained results (Table 2 are compared with the simplified thermal distribution function LBM implementation of Peng et al. (2003), and the results from a differential quadrature implementation (noted as *DQ* in the table) of the Navier Stoke's equations by Shu et al. (1997).

Table 2. Comparison of convection velocities for various values of *Ra.*

Ra		10^3 101×101	10^4 151×151	10^5 201×201	10^6 251×251
u_{max}	Current	3.712	16.275	33.557	60.600
	Peng	3.644	16.146	34.261	63.671
	DQ	3.649	16.190	34.736	64.775
y	Current	0.810	0.820	0.855	0.855
	Peng	0.810	0.820	0.855	0.852
	DQ	0.815	0.825	0.855	0.850
v_{max}	Current	3.752	19.748	69.058	224.52
	Peng	3.691	19.593	67.799	217.57
	DQ	3.698	19.638	68.640	220.64
x	Current	0.180	0.120	0.065	0.040
	Peng	0.180	0.120	0.065	0.040
	DQ	0.180	0.120	0.065	0.035
$\overline{Nu}$	Current	1.132	2.253	4.524	8.756
	Peng	1.117	2.241	4.511	8.737
	DQ	1.118	2.245	4.523	8.762

The maximum value of the x velocity component, u_{max}, and its y position at a static x location of $x = \frac{L}{2}$, where is L is the length of the channel, is recorded. In the same way, the maximum value of the y velocity component, v_{max}, and its x position at a static y location of $y = \frac{H}{2}$, where H is the height of the channel, is recorded. The corresponding average Nusselt number is also presented for each case. The isotherms and velocity streamlines are presented in Figure 4 and Figure 5, respectively. The results show very good agreement with both previous LBM and NS simulations.
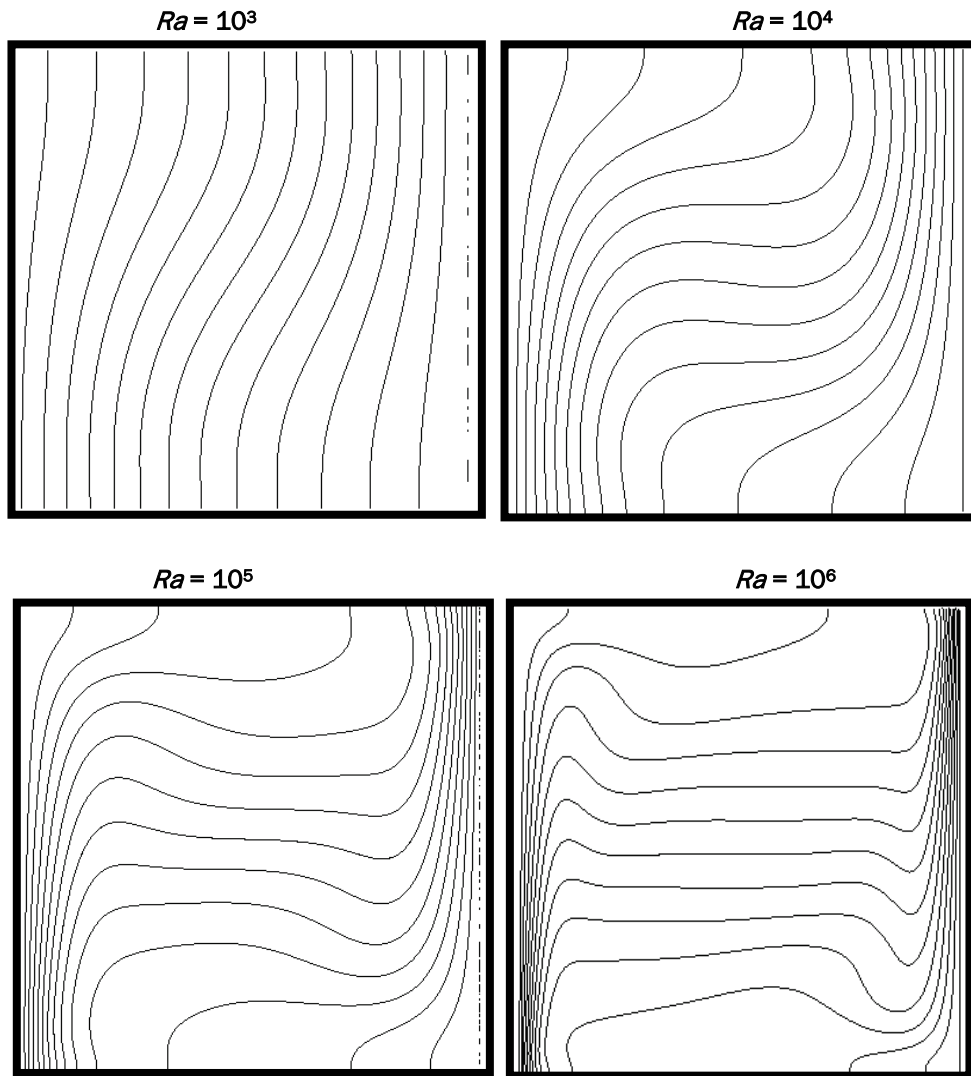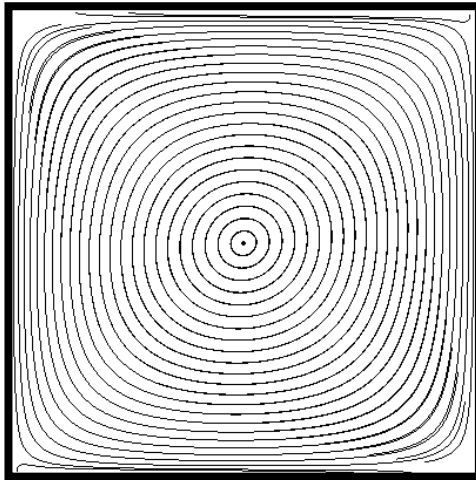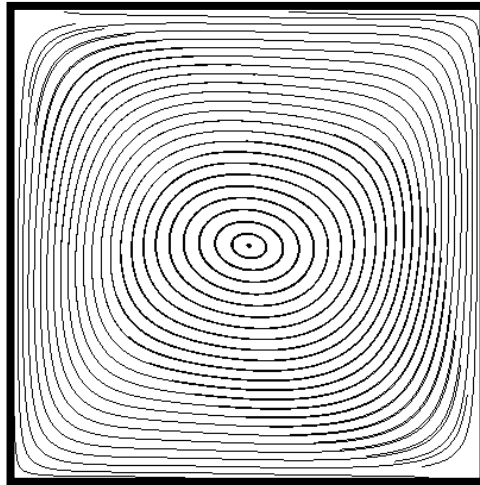
Figure 4. Isotherms for various values of Ra

$Ra = 10^3$

$Ra = 10^4$

$Ra = 10^5$

$Ra = 10^6$

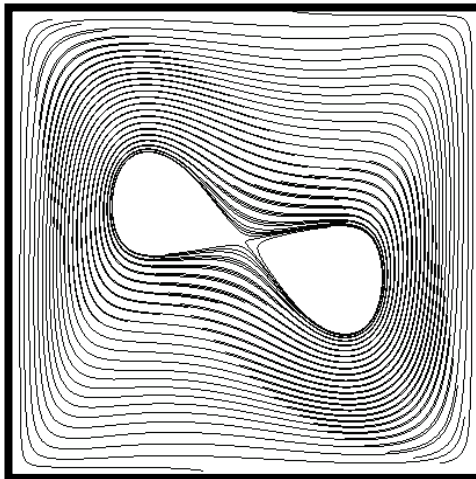Figure 5. Velocity streamlines for various values of *Ra*.

$Ra = 10^3$

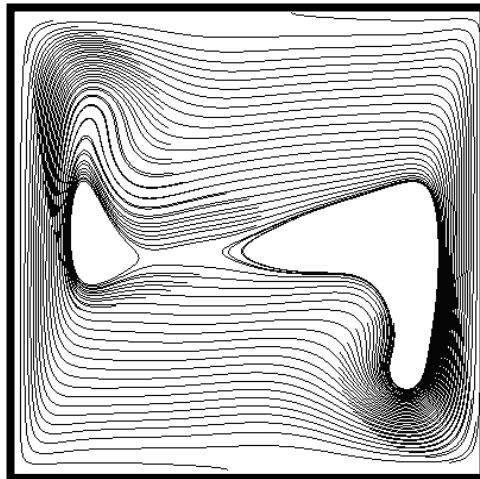$Ra = 10^4$

$Ra = 10^5$

$Ra = 10^6$

4   Microflow Interactions

Due to the difficulty of simulating microscale interactions with popular NS based fluid solvers (Lim et al. 2002; Niu et al. 2004), an extension to the LBM able to capture rarefaction effects is introduced (note this implementation is able to incorporate such effects solely by means of an increase in *Kn* and implementation of Diffuse Scattering Boundary Conditions to calculate the slip velocity with respect to a solid-fluid interface characteristic to microscale flows). For traditional macroscopic flows, rarefaction effects on the microscale are usually considered negligible and are omitted in practice. To measure microscale interactions, the Knudsen number, *Kn*, is employed, being a dimensionless parameter, defined as the ratio of a particle's mean free path to the characteristic length of the channel. As the Knudsen number increases (i.e., the mean free path is on the order of the characteristic length), particulate interactions must be considered. This ensures that traditional Navier-Stokes solvers are generally unable to yield accurate results in the transitional regime ($0.1 \leq Kn \leq 1$) due to modeling a fluid as continuum with continuous macroscopic quantities. However, microscale interactions must be studied with emphasis on rarefaction effects with discrete macroscopic quantities (Allen 2006). The LBM is an attractive method for microscopic fluid flow study due in part to the lack of an assumed continuum flow constraint, as well as a straightforward implementation of the Diffuse Scattering Boundary Conditions, able to expose slip velocity in rarefied gas flows. Further, the use of non-constant collision frequency allows direct implementation of microscale interactions.

Among the rarefaction effects to be modeled at the microscale is the existence of a Knudsen layer which exhibits non-equilibrium effects at the boundary and spans about the distance of one mean free path from the fluid-solid interface. This layer is formed due to the heightened frequency of particle collisions at the boundary (Homayoon et al. 2011) and creates a slip velocity at the fluid-solid interface expressed as the particle's velocity relative the boundary velocity. For higher *Kn*, the effects of the Knudsen layer are a dominant effect in the flow. Further, collisions at boundaries are reflected in a manner slightly inconsistent with the equilibrium state described by the Maxwellian distribution function. Certain treatments must be implemented for accurate simulation of a Knudsen layer, as well

as boundary conditions able to describe fluid-boundary collisions. (Lilley and Sader, 2008)

A variety of proposals exist to effectively tie the LBM with accurate microchannel representation. Among these are the introduction of *effective* quantities as employed by Ghazanfarian and Abbassi (2010) and Homayoon et al. (2011), and are written in terms of the originally calculated quantities. Hoyamoon et al. (2011) proposed an effective dynamic viscosity that yields an effective relaxation time where both parameters were inversely proportional to some function of *Kn*. Lim et al. (2002) introduced an updated *Kn* inversely proportional to the pressure distribution in the channel effectively updating the relaxation time due to the assumption that the channel pressure is proportional to the mean free path and the mean free path is proportional to the relaxation time. Niu et al. (2004) presented $\tau_v \propto Kn$ modified by the specific heat ratio for a monatomic gas.

Of greatest significance though, is that most authors agree that the dimensionless relaxation time is proportional to the Knudsen number since $\tau_v \propto Kn$ (Ghazanfarian and Abbassi 2010; Homayoon et al. 2011; Lim et al. 2002; Niu et al. 2004). Therefore, the introduction of a fixed *Kn* is directly reflected in an update of the collision frequency.

Letting λ represent the mean free path of the considered particles and H be the characteristic length of the channel, here representing the channel height, the Knudsen number is given by

$$Kn = \frac{\lambda}{H} \tag{49}$$

The mean free path can then by calculated by $\lambda = \langle v \rangle \Theta$, where $\langle v \rangle$ is the average magnitude of velocity of the particles enclosed in the system given by $\langle v \rangle = \sqrt{\frac{8RT}{\pi}}$ and Θ is the relaxation time related to τ_v by $\Theta = \tau_v \delta_t$. (Niu et al. 2004) In the D2Q9 model, $\langle v \rangle$ is transformed by $c = \sqrt{3RT}$ to $\langle v \rangle = c\sqrt{\frac{8}{3\pi}}$. Thus, writing λ in terms of τ_v yields

$$\lambda = c\sqrt{\frac{8}{3\pi}} \tau_v \delta_t \tag{50}$$

The characteristic length is then given by

$$H = N_H \delta_x \tag{51}$$

where N_H is the number of lattice sites that span the width of the channel and δ_x is the lattice site spacing and is assumed to be constant throughout. From Equation 50 and Equation 51, the evaluation of Kn can be updated, yielding:

$$Kn = c\sqrt{\frac{8}{3\pi}} \frac{\tau_v \delta_t}{N_H \delta_x} \tag{52}$$

Noting that $c = \frac{\delta_x}{\delta_t}$ and implementing a correction factor of $-\frac{1}{2}$ to maintain second order accuracy (in accordance with with the Chapman-Enskog analysis (Ghazanfarian and Abbassi 2010)), Equation 52 becomes

$$Kn = \sqrt{\frac{8}{3\pi}} \frac{\tau_v - \frac{1}{2}}{N_H} \tag{53}$$

The Kn has now been effectively tied to relaxation time as assumed by the present authors. With this formalization of Kn for the D2Q9, the relaxation time can now be determined in terms of a desired Kn. With the calculated τ, λ can also be computed by Equation 50. In order to ensure a more accurate Knudsen layer, Ghazanfarian et al. (2010) proposed a wall function that modifies λ in Equation 50 by

$$\lambda_e = \frac{\lambda}{1 + \psi\left(\frac{y}{\lambda}\right) + \psi\left(\frac{H-y}{\lambda}\right)} \tag{54}$$

where ψ is given by $\psi(x) = e^{-Cx}$, C is a constant set to unity in this work, Pr is the previously introduced Prandtl number and y is the normal distance relative to the bottom wall. Further, Ghazanfarian and Abbassi (2010) also formulated a modification to τ_v in attempt to couple the contributions generated by the density and internal energy distribution functions that is given by

$$\tau_v' = \frac{\tau_v - \frac{1}{2}}{1 + \psi\left(\frac{y}{\lambda}\right) + \psi\left(\frac{H-y}{\lambda}\right)} \frac{\rho_{ref}}{\rho}\left(\frac{\epsilon}{\epsilon_{ref}}\right)^{\omega - \frac{1}{2}} + \frac{1}{2} \tag{55}$$

Note that τ_v' is written in terms of τ_v, ϵ, and ρ. This calculation considers the desired microscale interactions through the implementation of τ_v derived from a chosen Kn, internal energy updated by thermal interactions, and pressure contributions due to the linear relationship of pressure and density in the LBM. Implementation of Equation 55 couples density and internal energy interactions in LBM allowing for both and pressure and thermal interactions to be simulated on the microscale.

Since $Pr = \frac{v}{\chi}$, $v \propto \tau_v$, and $X \propto \tau_c$, the thermal relaxation time can then be computed in terms of Pr as

$$\tau_c = \frac{\tau_v - \frac{1}{2}}{Pr} + \frac{1}{2} \tag{56}$$

4.1 Boundary conditions

To correctly model the slip velocity on the walls, the standard bounceback condition is shifted to a discretized Maxwell boundary condition, referred to as the DSBC. The DSBC as presented (Tang et al. 2005) is shown and was implemented in this work.

With knowledge of the wall velocity, the motion of the particles near the wall can be expressed with slip reference velocity of $\vec{\xi}_i = \vec{c}_i - \vec{u}_w$. The reference velocity projection over the unit normal to the wall is then given as $\vec{\xi}_i \cdot \vec{n}$, where $\vec{n}$ is the normal unit vector pointing into the flow. With the values of $\vec{\xi}_i \cdot \vec{n}$, the respective f_i can be grouped into three sets. Particles with values of $\vec{\xi}_i \cdot \vec{n} < 0$ must be incident to the wall and are grouped in I_i. Particles with $\vec{\xi}_i \cdot \vec{n} > 0$ are reflected particles and are placed in I_r. Finally, particles with $\vec{\xi}_i \cdot \vec{n} = 0$ must be "grazing" particles and are placed in I_g.

In this grouping, information about incident and grazing particles are already known and the reflected particles must be solved for. According to kinetic theory, the reflected particle distribution function is related to that of the incident particles by (Struchtrup 2013)

$$f_{j \in I_r} = \frac{1}{\left\| \left(\vec{\xi}_j \cdot \vec{n} \right) \right\|} \int\limits_{i \in I_i}^{i_{tot}} f_i \mathcal{R} \left(\vec{c}_i \to \vec{c}_i^{'} \right) \left\| \left(\vec{\xi}_i \cdot \vec{n} \right) \right\| \tag{57}$$

Here $\mathcal{R}(\vec{c}_i \to \vec{c}_i^{'})$ is the scattering kernel which represents the probability that particles which hit the boundary with velocity $\{c_k^{'}, c_k^{'} + dc^{'}\}$ will return to the flow with velocity $\{c_k, c_k + dc^{'}\}$. Due to the consideration of only nonporous and nonabsorbent boundaries, the normalization constraint for $\mathcal{R}(\vec{c}_i \to \vec{c}_i^{'})$ yields (Struchtrup 2013; Tang et al. 2005)

$$\int\limits_{i \in I_i}^{i_{tot}} \mathcal{R} \left(\vec{c}_i \to \vec{c}_i^{'} \right) d\vec{c} = 1 \tag{58}$$

which guarantees that all boundary colliding particles are returned to the flow. For purposes in the LBM, discretization of Equation 57 is written as

$$\left(\vec{\xi}_j \cdot \vec{n} \right) f_j = \sum_{i \in I_i} - \left(\vec{\xi}_i \cdot \vec{n} \right) \mathcal{R}_{ij} f_i \tag{59}$$

In attempt to represent multiple particle-boundary interactions, various formulations of $\mathcal{R}$ are considered by kinetic theory. In his model, Maxwell chose to consider the specular and diffusive derivations of $\mathcal{R}$ and couple them linearly with the tangential momentum accommodation coefficient, σ_v, such that $\sigma_v \in [0, 1]$ by applying σ_v to the diffuse condition and $\sigma_v - 1$ to the specular condition. Considering the specular and diffusive boundary conditions, the DSBC in the LBM may be expressed as

$$f_j \left(\vec{x}, t + \hat{\delta}_t \right) = (1 - \sigma_v) f_{j'} \left(\vec{x}, t + \hat{\delta}_t \right) \left(\vec{\xi}_j \cdot \vec{n} \right) +$$
$$\sigma_v \frac{\sum_{i \in I_i} - \left(\vec{\xi}_i \cdot \vec{n} \right) f_i \left(\vec{x}, t + \hat{\delta}_t \right)}{\sum_{j \in I_j} \left(\vec{\xi}_j \cdot \vec{n} \right) f_j^{eq} \left(\vec{x}, \rho_w, \vec{u}_w, t + \hat{\delta}_t \right)} f_j^{eq} \left(\vec{x}, \rho_w, \vec{u}_w, t + \hat{\delta}_t \right) \tag{60}$$

where $j \in I_r$. Note that taking $\sigma_v = 1$ considers the particle reflection to be completely diffusive and $\sigma_v = 0$ takes the particle reflection to be completely specular. In this work, the value of $\sigma_v = 1$ is exclusively considered. The diffusive interaction ensures that incoming particles are reflected in such a way that the particle "loses its memory" of its incoming direction and is after scattered such that both the tangential and normal components of its direction are altered. (Niu et al. 2006; Struchtrup 2013; Tang et al. 2005) It

has also been shown by Niu et al. (2006) that for steady flow where the velocity varies only the streamwise-normal direction the slip velocity may written in terms of only Kn and $\vec{u}$.

4.2 Validation

Correct implementation of microchannel support for the LBM was validated through simulation of Poiseuille flow with heated walls over a set of fixed Kn. A strong pressure gradient of ratio 2 across the channel is implemented using the enforced density boundary condition proposed by Zou et al. (1997). In the work, $\frac{P_1}{P_2} = 2$, with P_1 being the inlet pressure and P_2 is the outlet pressure. The velocity is then calculated in order to maintain the desired pressure. At the north and south walls, the velocity condition in Equation 37 was first applied to ensure the wall velocity was zero and then DSBC conditions were applied. Due to the DSBC, the presence of a slip velocity was observed as expected for microscale flows.

The bottom and top walls have an imposed internal energy of ϵ_1 and ϵ_2, respectively, with an internal energy ratio corresponding to $\frac{\epsilon_1}{\epsilon_2} = 2$. At the inlet, the internal energy is as measured with respect to the top wall is $\frac{\epsilon_{in}}{\epsilon_2} = 1.5$. To enforce the internal energy on the walls, the thermal boundary condition presented in Equations 39–42 are used by first determining the known temperature from the internal energy with $\epsilon = RT$.

To enforce the effects of the Knudsen layer, the wall function modification of λ shown in Equation 54 is implemented. The adjustment of τ_ν by Equation 55 is also implemented, effectively coupling the microchannel and thermal interactions. With the use of Equation 55, the viscosity and thermal diffusivity are now both dependent on pressure and internal energy. Due to this, it can be observed that the pressure distribution is no longer linear. The pressure is presented after being normalized by $\frac{P-P_l}{P_2}$ where P_l is the expected linear pressure distribution given in terms of $x^* = \frac{x}{L}$ with L being the length of the channel by $P_l = P_1 + x^*(P_2 - P_1)$. Deviation from linear pressure is compared to the results found by Ghazanfarin and Abbassi (2010) and is presented for various Kn in Figure 6.

To demonstrate the validity of the implemented model, comparisons of velocity profiles normalized by the bulk velocity are presented for various Kn. The presented results are compared with those produced by

Ghazanfarian and Abbassi (2010) and are shown in Figures 6–9. Due to thermal-microscale coupling, the velocity is updated depending on pressure, internal energy, and Knudsen layer modeling, making the velocity profiles an interesting calculation. It is seen that the yielded results agree very well with those presented by Ghazanfarian and Abbassi (2010).

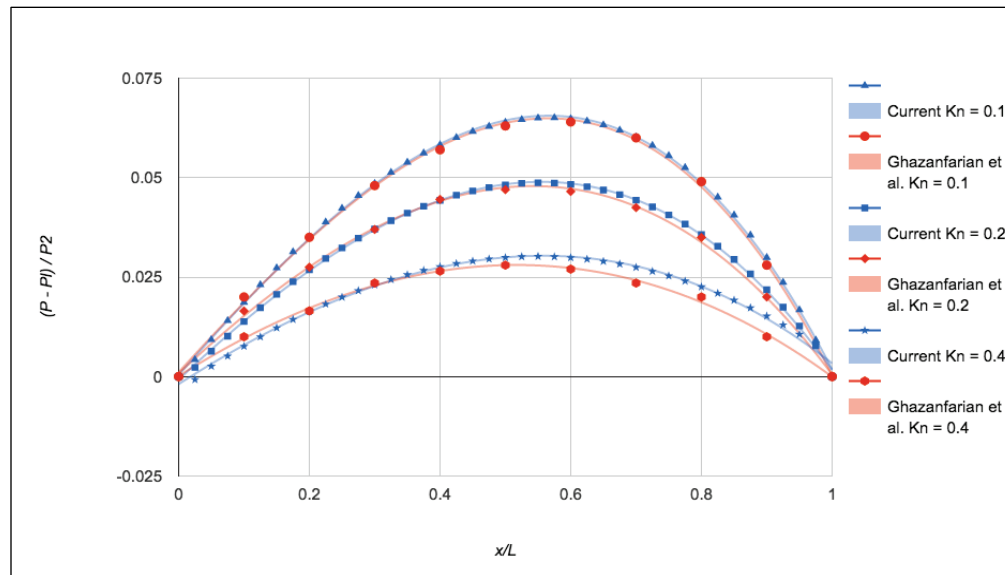Figure 6. Deviation from linear pressure distribution for various *Kn.*

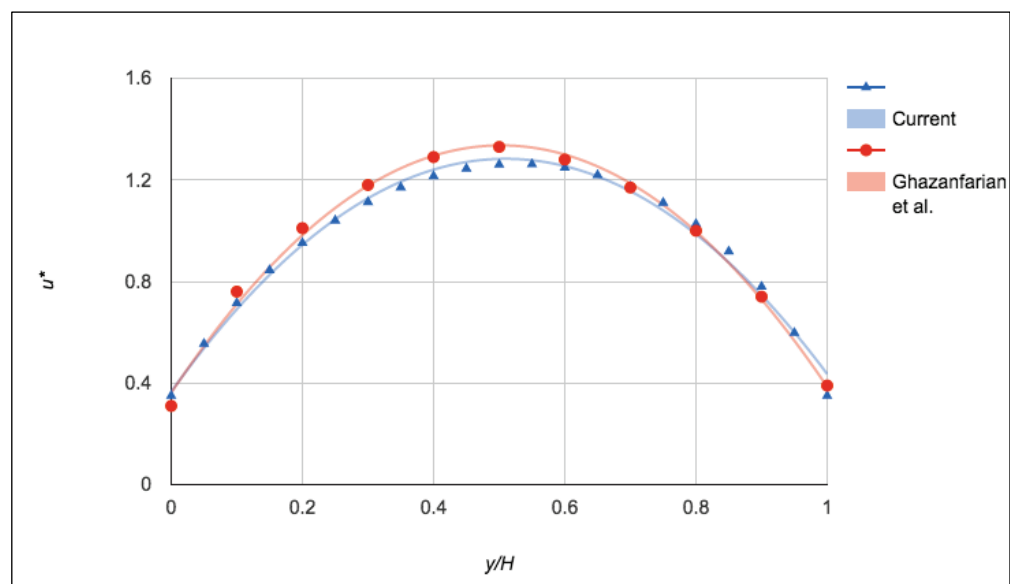Figure 7. Normalized velocity profile corresponding to *Kn* = 0.1.

Figure 8. Normalized velocity profile corresponding to *Kn* = 0.2.
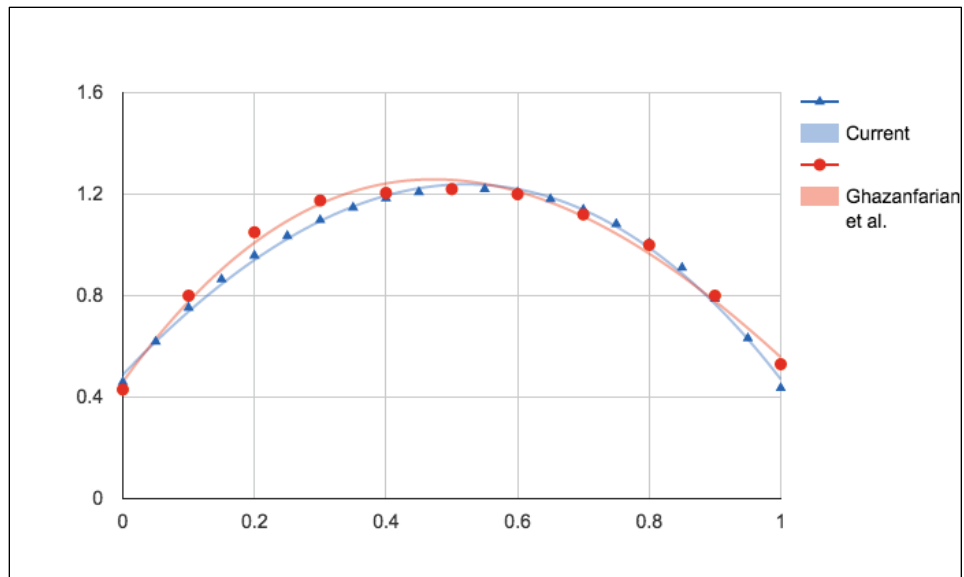
Figure 9. Normalized velocity profile corresponding to *Kn* = 0.4.
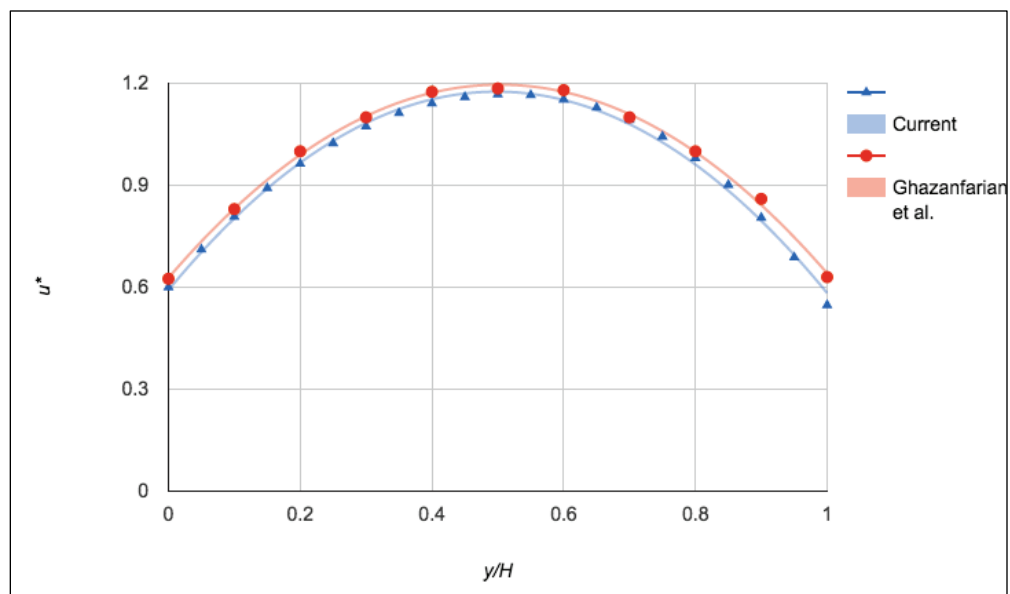
5 Summary

This report demonstrated the validity of various physical extensions implemented within the LBM. It was shown, through a variety of worked examples, that the LBM is able to accurately account for flows around complex immersed boundaries, thermal convection driven flows, and microchannel flows. Further, this effort also served to set the LBM apart as a computationally accurate method, especially for microscale flow scenarios. In particular, this accuracy was demonstrated in simulations of (1) flow around an immersed cylinder, (2) natural convection in a square channel, and (3) pressure driven flow with heated walls and Knudsen layer accommodation. Of particular interest is the effective coupling of thermal and microchannel support. Given the present work as a foundation, future efforts may focus on particulate flows through microscale electronics, deformation and heat transfer of grain-structured materials, and rarefaction effects on microscale boundaries.

References

Allen, J. B., W. D. Hodo, L. Walizer, D. Mcinnis, A. Carrillo, B. Jelenik, D. Johnson, J. Peters, and S. D. Felicelli. 2014. *Comparison/Validation study of Lattice Boltzmann and Navier-Stokes for various benchmark applications*. ERDC TR-14-6. Vicksburg, MS: U.S. Army Engineer Research and Development Center.

Allen, J. B. 2006. Direct simulation monte carlo simulations of aerodynamic effects on sounding rockets. PhD Diss., Utah State University.

Feng, Z. G., and E. E. Michaelides. 2003. The immersed boundary-lattice Boltzmann method for solving fluid-particles interaction problems. *Journal of Computational Physics* 195:602–628.

Ghazanfarian, J., and A. Abbassi. 2010. Heat transfer and fluid flow in microchannels and nanochannels at high Knudsen number using thermal lattice-Boltzmann method. *Physical Review E* 82(2).

Guo, Z., C. Zheng, and B. Shi. 2007. Thermal lattice Boltzmann equation for low Mach number flows: Decoupling model. *Physical Review E* 75(3).

He, X., S. Chen, and G. D. Doolen. 1998. A Novel Thermal Model for the Lattice Boltzmann Method in Incompressible Limit. *Journal of Computational Physics* 146(1):282–300.

Homayoon, A., A. M. Isfahani, E. Shirani, and M. Ashrafizadeh. 2011. A novel modified lattice Boltzmann method for simulation of gas flows in wide range of Knudsen number. *International Communications in Heat and Mass Transfer* 38(4):827–832.

Lilley, C. R., and J. E. Sader. 2008. Velocity profile in the Knudsen layer according to the Boltzmann equation. In *Proceedings of the Royal Society of London A: Mathematical, Physical, and Engineering Sciences* 464(2096):2015–2035. The Royal Society.

Lim, C. Y., C. Shu, X. D. Niu, and Y. T. Chew. 2002. Application of lattice Boltzmann method to simulate microchannel flows. *Physics of Fluids* 14(7):2299–2308.

Liu, C. H., K.-H. Lin, H. C. Mai, and C. A. Lin. 2010. Thermal boundary conditions for thermal lattice Boltzmann simulations. *Computers and Mathematics with Applications* 59:2178–2193

McNamara, G. R., A. L. Garcia, and B. J. Adler. 1995. Stabilization of Thermal Lattice Boltzmann Models. *Journal of Statistical Physics* 81(1):395–408.

Mohamad, A. A., and A. Kuzmin. 2010. A critical evaluation of force term in lattice Boltzmann method, natural convection problem. *International Journal of Heat and Mass Transfer* 53:990–996.

Niu, X. D., C. Shu, and Y. T. Chew. 2004. A lattice Boltzmann BGK model for simulation of micro flows. *Europhysics Letters* 67(4):600–606.

Niu, X. D., C. Shu, Y. T. Chew, and Y. Peng. 2006. A momentum exchange-based immersed boundary-lattice Boltzmann method for simulating incompressible viscous flows. *Physical Letters A* 354:173–182.

Niu, X. D., C. Shu, and Y. T. Chew. 2006. A thermal lattice Boltzmann model with diffuse scattering boundary condition for micro thermal flows. *Computers & Fluids* 36:373–381.

Nor Azwadi, C. S., and T. Tanahashi. 2006. Simplified thermal lattice Boltzmann in incompressible limit. *International Journal of Modern Physics B* 20(17):2437–2449.

Peng, Y., C. Shu, and Y. T. Chew. 2003. Simplified thermal lattice Boltzmann model for incompressible thermal flows. *Physical Review E* 68(2).

Peskin, C. S. 2002. The immersed boundary method. *Acta Numerica* 11:479–517. doi: https://doi.org/10.1017/S0962492902000077.

Shan, X. 1997. Solution of Rayleigh Bénard convection using a lattice Boltzmann method. *Physical Review E* 55:2780–2788.

Shu, C., and H. Xue. 1997. Comparison of two approaches for implementing stream function boundary conditions in DQ simulation of natural convection in a square cavity. *International Journal of Heat and Fluid Flow* 19:59–68.

Struchtrup, H. 2013. Maxwell boundary condition and velocity dependent accommodation coefficient. *Physics of Fluids* 25(11).

Tang, G. H., W. Q. Tao, and Y. L. He. 2005. Lattice Boltzmann method for gaseous microflows using kinetic theory boundary conditions. *Physics of Fluids* 17(5):058101.

Zou, Q., and X. He. 1997. On pressure and velocity boundary conditions for the lattice Boltzmann BGK model. *Physics of Fluids* 9(6):1591–1598.

Appendix A: Discretized Delta Function Validation

Consider a Lagrange marker located at $\vec{X}_s = (x_i + \Delta x, y_j + \Delta y)$ where $\vec{r}_{ij} = (x_i, y_j)$ is the nearest lower left Eulerian marker relative to $\vec{X}_s$ and $x_i \geq \Delta x > x_{i+1}$, $y_j \geq \Delta y > y_{j+1}$. If the force at the Eulerian nodes is updated by Equation 8 and applied to a domain Ω, the magnitude of force distributed to $\vec{r}_{ij}$ is given by

$$\sum_{i=1}^{n} \delta_h (i - n + 1 + \Delta x) \sum_{j=1}^{n} \delta_h (j - n + 1 + \Delta y) \tag{A1}$$

Let α be the first summation and β the second summation, such that $\alpha = \sum_{i=1}^{n} \delta_h (i - n + 1 + \Delta x)$ and $\beta = \sum_{j=1}^{n} \delta_h (j - n + 1 + \Delta y)$. Note that terms above $n = 4$ equal 0. Expanding α, we find

$$\alpha = \delta_h(-2 + \Delta x) + \delta_h(-1 + \Delta x) + \delta_h(\Delta x) + \delta_h(1 + \Delta x) \tag{A2}$$

Evaluating first term of α yields

$$\delta_h(-2 + \Delta x) = \frac{1}{4} \left[1 + \cos\left(\frac{-2\pi}{2} + \frac{\Delta x \pi}{2} \right) \right] \tag{A3}$$

Applying the trigonometric identity for $\cos(a + b)$, we find Equation A3 evolves into Equation A4

$$\delta_h(-2 + \Delta x) = \frac{1}{4} \left[1 + \cos\frac{-2\pi}{2} \cos\frac{\Delta x \pi}{2} - \sin\frac{-2\pi}{2} \sin\frac{\Delta x \pi}{2} \right] \tag{A4}$$

After following this procedure of evaluating the delta function and applying the trigonometric identity for $\cos(a + b)$ for the remaining three terms in α, we group terms and find

$$\alpha = \frac{1}{4}\left[\begin{array}{c}4+\cos\dfrac{\Delta x\pi}{2}\left(\cos\dfrac{-2\pi}{2}+\cos\dfrac{-\pi}{2}+\cos\dfrac{0\pi}{2}+\cos\dfrac{\pi}{2}\right)\\[2ex]-\sin\dfrac{\Delta x\pi}{2}\left(\sin\dfrac{-2\pi}{2}+\sin\dfrac{-\pi}{2}+\sin\dfrac{0\pi}{2}+\sin\dfrac{\pi}{2}\right)\end{array}\right] \quad \text{(A5)}$$

Evaluating the four inner cosines and sines proves that $\alpha = 1$ for all Δx. This same procedure can be applied for β and it becomes apparent that $\beta = 1$ as well. Therefore, $\alpha\beta = 1$ for enclosed discretized Eulerian markers independent of the location of the forcing Lagrange marker at $\vec{X}_s$.

Appendix B: Definition of Mathematical Symbols Used in LBM

Table B1. Definition of Mathematical Symbols used in LBM.

Symbol	Definition	Units
f^{eq}	density equilibrium distribution function	
D	dimension	
H	domain height	
L	domain length	
F	external force	
$\vec{u}$	fluid velocity	
$\vec{c}$	lattice velocity	
w_i	lattice weights	
$\vec{x}$	position vector	
p	pressure	
c_s	speed of sound	
t	time	
Greek		
τ_v	density distribution relaxation time	
ρ	fluid density	
v	kinematic viscosity	
δ_x	spatial discretization step	
δ_t	temporal discretization step	

Appendix C: Definition of Mathematical Symbols Used in IMB

Table C1. Definition of Mathematical Symbols used in IMB.

Symbol	Definition	Units
C_D	drag coefficient	
F_r	force reapplied to flow	
$\vec{F}_s$	immersed boundary body force	
I_o	immersed boundary moment of inertia	
T_o	immersed boundary torque	
$\vec{X}$	Lagrangian node position	
m	mass	
$\vec{X}_{cm}$	object center of mass	
D_{ij}	2D lattice force mollifier	
Greek		
ω	angular velocity	
δ_h	force distribution mollifier	

Appendix D: Definition of Mathematical Symbols Used in Thermal Interactions

Table D1. Definition of Mathematical Symbols used in Thermal Interactions.

Symbol	Definition	Units
g_0	acceleration due to gravity	
T_m	average temperature	
R	gas constant	
T	temperature	
g^{eq}	thermal equilibrium distribution function	
q	viscous heating and compression contribution	
ΔT	wall temperature difference	
Greek		
ε	internal energy	
Π	stress tensor	
X	thermal diffusivity	unitless
τ_c	thermal distribution relaxation time	unitless
β	thermal expansion coefficient	unitless

Appendix E: Definition of Mathematical Symbols Used in Microflow Interactions

Table E1. Definition of Mathematical Symbols used in Microflow Interactions

Symbol	Definition	Units
N_H	characteristic length	
$\mathcal{R}$	scattering kernel	
Greek		
$\vec{\xi}$	fluid-wall relative velocity	
λ	mean free path	unitless
Θ	relaxation time	s^{-1}
σ_v	tangential momentum accommodation coefficient	unitless

REPORT DOCUMENTATION PAGE		*Form Approved* *OMB No. 0704-0188*

Public reporting burden for this collection of information is estimated to average 1 hour per response, including the time for reviewing instructions, searching existing data sources, gathering and maintaining the data needed, and completing and reviewing this collection of information. Send comments regarding this burden estimate or any other aspect of this collection of information, including suggestions for reducing this burden to Department of Defense, Washington Headquarters Services, Directorate for Information Operations and Reports (0704-0188), 1215 Jefferson Davis Highway, Suite 1204, Arlington, VA 22202-4302. Respondents should be aware that notwithstanding any other provision of law, no person shall be subject to any penalty for failing to comply with a collection of information if it does not display a currently valid OMB control number. **PLEASE DO NOT RETURN YOUR FORM TO THE ABOVE ADDRESS.**

1. REPORT DATE *(DD-MM-YYYY)* July 2017	2. REPORT TYPE Report 2 of a series	3. DATES COVERED *(From - To)*

4. TITLE AND SUBTITLE	5a. CONTRACT NUMBER
Thermal, Microchannel, and Immersed Boundary Extension Validation for the Lattice-Boltzmann Method: Report 2 in "Discrete Nano-Scale Mechanics and Simulations" Series	5b. GRANT NUMBER
	5c. PROGRAM ELEMENT NUMBER

6. AUTHOR(S)	5d. PROJECT NUMBER
William P. England and Jeffrey B. Allen	5e. TASK NUMBER
	5f. WORK UNIT NUMBER #MR014

7. PERFORMING ORGANIZATION NAME(S) AND ADDRESS(ES)	8. PERFORMING ORGANIZATION REPORT NUMBER
U.S. Army Engineer Research and Development Center Information Technology 3909 Halls Ferry Road, Vicksburg, MS 39180-6199	ERDC TR-14-6

9. SPONSORING / MONITORING AGENCY NAME(S) AND ADDRESS(ES)	10. SPONSOR/MONITOR'S ACRONYM(S)
Headquarters, U.S. Army Corps of Engineers Washington, DC 20314-1000	11. SPONSOR/MONITOR'S REPORT NUMBER(S)

12. DISTRIBUTION / AVAILABILITY STATEMENT

Approved for public release; distribution unlimited.

13. SUPPLEMENTARY NOTES

14. ABSTRACT

The Lattice Boltzmann Method continues to garner interest in fluids research, particularly with its ability to accurately simulate laminar flows in the incompressible region. This interest can be attributed in part to the ease of implementation the Lattice Boltzmann Method provides; including a lack of complex differential terms and a linear approximation of the collision operator contained in the Boltzmann equation. In this work, the traditional Lattice Boltzmann solver is augmented with support for immersed boundaries, thermal flows, and microchannel flows. Thermal and micro-enabling support is demonstrated and validated through Rayleigh convection in a square channel and thermally coupled Poiseuille flow through a microchannel, respectively.

15. SUBJECT TERMS	Lattice Boltzmann methods Fluid dynamics Laminar flow	Kinetic theory of liquids Boundary value problems Heat--Transmission

16. SECURITY CLASSIFICATION OF:			17. LIMITATION OF ABSTRACT	18. NUMBER OF PAGES	19a. NAME OF RESPONSIBLE PERSON
a. REPORT UNCLASSIFIED	**b. ABSTRACT** UNCLASSIFIED	**c. THIS PAGE** UNCLASSIFIED		46	19b. TELEPHONE NUMBER *(include area code)*

Standard Form 298 (Rev. 8-98)
Prescribed by ANSI Std. 239.18